

# A microstructural approach to bedload transport: spatio-temporal fluctuations of the particle activity.

J. Heyman<sup>1</sup>, H.B. Ma<sup>2</sup>, F. Mettra<sup>1</sup> and C. Ancey<sup>1</sup>

**Abstract.** This article examines the spatial and temporal behaviors of the dynamics of bedload particles in water. We focus particularly on the fluctuations of particle activity, defined as the number of moving particles per unit bed area. Based on a stochastic model recently proposed by the authors [Ancey and Heyman, 2013], we derive the second order moments of particle activity analytically; that is the spatial and spatio-temporal correlation functions of particle activity. From these expressions, we show that fluctuations of particle activity in space depend greatly on the scale of observation. To link spatial fluctuations to temporal fluctuations, we consider the validity of Taylor’s frozen-flow hypothesis. Three different experimental data sets are used to test the theoretical results and the hypothesis. We provide a general method to find model parameters based on experimental data. We show that the stochastic model described spatial patterns of particle activity well at all scales. However, we demonstrate that the frozen-flow hypothesis proves to be inaccurate for most of the experiments.

## 1. Introduction

Born in the late 1930s with the seminal work of Hans Albert Einstein [Einstein, 1937, 1950], the stochastic approach to bedload transport has had a surge of interest among the scientific community in recent years [Papanicolaou et al., 2002; Jerolmack and Mohrig, 2005; Ancey et al., 2008, 2006; Valyrakis et al., 2010; Ancey, 2010; Furbish and Schmeeckle, 2013]. This revival has been combined with a substantial improvement in laboratory measurement techniques. In particular, the use of high-speed films of particle motion together with powerful digital processing, has allowed for groundbreaking precision in the description of sediment particle dynamics [Roseberry et al., 2012; Martin et al., 2012; Lajeunesse et al., 2010; Böhm et al., 2004].

The major advantage of a stochastic framework compared to a classic description of sediment transport lies in the information it gathers about first and higher order moments (for instance the variance). This advantage is particularly suited to bedload transport rates, which are known to often show fluctuations much larger than the mean [Singh et al., 2009; Ancey et al., 2006; Hoey, 1992; Drake et al., 1988; Kuhnle and Southard, 1988].

Among the recent studies on stochastic sediment transport, Ancey et al. [2008] developed a model describing the fluctuations in the number of moving particles in an observation window, based upon their observations of an simplified particle flow experiment. They showed that the large fluctuations in the number of moving particles could be explained by a “collective” effect on the entrainment of particles. Furbish et al. [2012a] provided insights into the random motion of particles and the consequences of this on macroscopic conservation equations. Based on a large set of experimental particle trajectories, they showed that particle activity (defined as the number of moving particles per unit bed

length) is associated with a diffusive flux due to particle velocity fluctuations.

From an other perspective, stochastic concepts are also applied to describe the interaction of turbulent fluid and bed particles. It is now widely accepted that, not only the mean fluid velocity, but also its fluctuating component is involved in particle entrainment [Papanicolaou et al., 2002; Valyrakis et al., 2010].

Most current stochastic theories for bedload transport avoid a complete mechanistic description of fluid-particle or particle-particle coupling, but assume basic random processes meant to represent them (e.g. probable entrainment of a particle by the turbulent fluid, change in its moving velocity) [Ancey et al., 2008; Lajeunesse et al., 2010]. Most of them also assume stationary and homogeneous transport conditions so that spatial fluctuations are ignored.

Ancey and Heyman [2013] recently proposed a model that allows the study of the spatial fluctuations of particle activity. By studying the erosion, deposition and motion of particles on a lattice made of regular cells, they ended up with an exact Fokker-Planck equation describing the process in both space and time. The model is valid for transport conditions ranging from low to moderate solid discharges. These conditions are often found in natural streams.

This paper aims to push forward Ancey and Heyman [2013] model by drawing on some of the major conclusions introduced by spatio-temporal variability in bedload activity. While Ancey and Heyman [2013] paper concerned the theoretical foundations of the model, this article focuses on practical issues. In doing so, we will demonstrate how the model reproduces the spatial and temporal fluctuations of the bedload activity. The second purpose of this paper is to test the model against various experimental data. These data include the description of particles trajectories in a time-space plane. At a given time, particle positions define a cloud of points in space that can be associated with a spatial point process [Cox and Isham, 1980]. Point processes have been extensively studied in sociology, biology, geography and many other fields of science [Baddeley, 2007; Jensen and Nielsen, 2001; Ogata, 1999] and a whole mathematical framework has been specially constructed for these discrete processes. The model proposed by Ancey and Heyman [2013] starts from a slightly different mathematical framework, known as Markov process [Gillespie, 1991]. However, the Poisson representation [Gardiner and Chaturvedi, 1977]

<sup>1</sup>Laboratory of Environmental Hydraulics, School of Architecture, Civil and Environmental Engineering, École Polytechnique Fédérale de Lausanne, Switzerland

<sup>2</sup>State Key Laboratory of Hydroscience and Engineering, Tsinghua University, Beijing, China

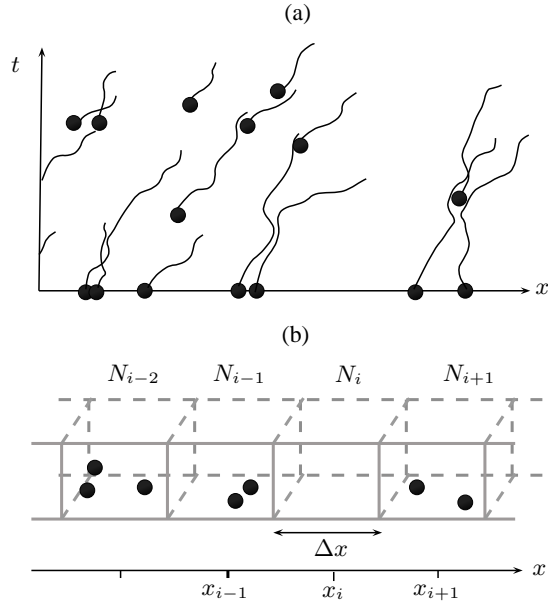


**Figure 1.** (a) Particle trajectories in a time-space plane. (b) Discretization of the space in cells of equal length  $\Delta x$  and counting the number of particles in each cell  $i$  at a given time  $t$ .

provides a nice link between the two approaches (i.e. point process and Markov process) that will be illustrated in this article.

The paper is organized as follows. First, to make the article self-contained, we briefly go over how the general stochastic equations governing the granular phase are derived and how the Poisson representation helps to simplify the equations. A rigorous and detailed derivation is not provided here since it has been extensively studied [Ancey and Heyman, 2013]. Next, we calculate the second-order moments (the spatial correlation function and the spatio-temporal correlation function) and show how they affect the variability of the bedload activity in both time and space. We also give the analytical expressions of the  $K$ -function [Ripley, 1976], a quantity used in point process analysis. Finally, we use three different experimental studies to test the model, two of which have already been published [Böhm et al., 2004; Roseberry et al., 2012]. The third study was recently carried out by the authors. A general method to calibrate model parameters on experimental data is proposed.

## 2. Theory

### 2.1. Physical space

The transport of bedload particles occurs in a thin layer over the surface of an erodible bed. Particles generally move in a preferential direction (down the slope, parallel to fluid flow) so that it is possible to restrain the study to a one-dimensional space in that principal direction. A generalization to a two-dimensional space, while technically possible, goes beyond the scope of this paper.

Let us consider a one-dimensional space that represents a river reach, or an experimental flume. The space is divided into cells of equal length  $\Delta x$ . Each cell of this lattice is labelled by an index  $i$ . We call  $N_i(t)$  the random variable describing the number of moving particles  $n_i$  in cell  $i$  at time  $t$ . Thus, we introduce the multivariate probability:

$$P([n_1, n_2, \dots], t) = P(\mathbf{n}, t), \quad (1)$$

where  $\mathbf{n}$  is the vector of all  $n_i$ . In other words,  $P(\mathbf{n}, t)$  is the probability of simultaneously observing  $N_1(t) = n_1, N_2(t) = n_2, \dots$ . Also,  $x_i$  denotes the position of the center of the cell  $i$ . The density of moving particles per unit bed length in cell  $i$ , also termed the particle activity, is  $\gamma(x_i, t) = N_i(t)/\Delta x$  [Furbish et al., 2012a].

### 2.2. Phenomenology

Bedload transport describes the motion of bed particles - sliding, rolling or saltating- sheared by a fluid. Ancey and Heyman [2013] distinguished three independent mechanisms involved in particle motions: entrainment, deposition and transport. These physical mechanisms are reviewed briefly below.

The entrainment of a resting particle by a fluid has been extensively studied and its random character is widely accepted [Dwivedi et al., 2011; Valyrakis et al., 2010; Celik et al., 2010; Detert et al., 2010; Wu and Chou, 2003; Papanicolaou et al., 2002; Einstein, 1950]. Certain experiments have suggested that other mechanisms of entrainment exist, such as collective entrainment by impact and destabilization [Ancey et al., 2008; Heyman et al., 2013], or by coherent turbulent fluid structures [Drake et al., 1988].

After being entrained, a particle is dragged by the fluid for a certain time before depositing onto the bed one more. The deposition rate, defined as the inverse of the travelling time [Lajeunesse et al., 2010], is highly sensitive to the properties of the turbulent fluid, bed packing, particle shape, dynamics of impact, etc. Thus, deposition is also considered to be a random process.

There is evidence that particles undergo dispersion during their motion, so that an initial cloud of moving particles will spread through space over short time periods [Nikora et al., 2002; Hill et al., 2010]. Diffusion in bedload transport is mainly due to particle velocity fluctuations. Starting from rest, an entrained particle accelerates to its maximum longitudinal velocity, but this will be frequently altered due to repeated impacts on the bed. Several cycles of acceleration and deceleration are frequently observed before a particle stops. Furbish and Schmeeckle [2013] proposed a model based on arguments from general statistical mechanics to explain the exponential behavior of the experimental density function of particle velocities [Lajeunesse et al., 2010; Roseberry et al., 2012]. Ancey and Heyman [2013] proposed a model of Brownian motion in a potential for the particle displacement and showing that particle velocities follow a truncated Gaussian distribution; this was consistent with their experimental data. Regardless of the form of the velocity distribution (providing that its second order moment exists) the resulting macroscopic effect on the particle activity flux is the sum of two contributions: an advective term and a diffusive term [Furbish et al., 2012a; Ancey and Heyman, 2013]. At the microscale, and under certain restrictive conditions [Ancey and Heyman, 2013], advection can be considered as a deterministic process, and diffusion as a random process.

### 2.3. Birth-death process and Poisson representation

To summarize the preceding phenomenological overview of the transport process, the probable random events (or reactions in the language of chemical engineering) modifying the value of  $N_i(t)$  are the following:



where  $\mu_i$  [ $\text{s}^{-1}$ ] is the collective entrainment rate in cell  $i$ ,  $\lambda_i$  [ $\text{particles}\cdot\text{m}^{-1}\text{s}^{-1}$ ] is the entrainment rate,  $\sigma_i$  [ $\text{s}^{-1}$ ] is the deposition rate and  $d_i$  [ $\text{s}^{-1}$ ] is the local diffusivity. Hereafter, homogeneity in space is assumed so that we can drop all rates indices  $i$ . Note that we did not consider the effect of the mean advection velocity in the cell boundary flux, because it is considered deterministic and will be reintroduced later in the equations.

From this birth-death Markov process, *Ancey and Heyman* [2013] derived the multivariate master equation for  $P(\mathbf{n}, t)$ . An exact solution of this master equation in terms of generating functions is unfortunately not tractable, except for the case of a single cell [*Ancey et al.*, 2008; *Heyman et al.*, 2013; *Ancey and Heyman*, 2013]. One usual procedure to simplify and solve a master equation relies on Van Kampen's expansion [*Van Kampen*, 2007]. However, the approximation involves a system size expansion that depends on the inverse of the cell size  $\Delta x$  (the smaller the system size, the worse the approximation).

*Gardiner and Chaturvedi* [1977] showed that a simpler stochastic equation can be obtained via the Poisson representation for discrete random variables. Similarly to Laplace or Fourier transforms in the spectral theory of time series, the Poisson representation is a linear operator that transforms a discrete probability space into a continuous one:

$$P(\mathbf{n}, t) = \prod_i \int_{\mathcal{C}} \frac{e^{-a_i} a_i^{n_i}}{n_i!} f(\mathbf{a}, t) da_i, \quad (3)$$

where  $a_i$  stands for the parameter of the Poisson distribution (its mean) while the function  $f(a_i, t)$  can be interpreted in some particular cases [*Gardiner*, 2002] as a density function representing the probability of observing an  $a_i$ -Poisson distribution in cell  $i$ . The transform allows one to solve the master equation by finding  $f(a_i, t)$ , which is a continuous random variable. The Fokker-Planck equation obtained for  $f(a_i, t)$  within this new space is strictly equivalent to the master equation and thus valid for all cell sizes [*Chaturvedi and Gardiner*, 1978; *Gardiner and Chaturvedi*, 1977].

Using the Poisson representation, *Ancey and Heyman* [2013] ended up with an explicit Langevin stochastic equation describing the transport of bedload particles:

$$da_i(t) = (d(a_{i+1} + a_{i-1} - 2a_i) - \lambda\Delta x - a_i(\sigma - \mu)) dt + \sqrt{2\mu a_i} dW_i(t), \quad (4)$$

where  $dW_i(t)$  is the derivative of a Wiener random process. This equation lays the foundation for the following analysis.

Just like the definition of the particle activity  $\gamma(x, t)$ , let us call  $\eta(x, t)$  the Poisson density variable, or Poisson activity. We have

$$\eta(x_i, t) = a_i(t)/\Delta x. \quad (5)$$

Using Eq. (1) and letting  $\Delta x \rightarrow 0$ , we obtain the Langevin stochastic partial differential equation in the Poisson density variable:

$$d\eta(x, t) = [D\nabla^2\eta(x, t) + (\mu - \sigma)\eta(x, t) + \lambda] dt + \sqrt{2\mu\eta(x, t)} dW(x, t), \quad (6)$$

where  $W(x, t)$  is now a spatial Wiener process with the correlation function:

$$dW(x, t)dW(x', t) = \delta(x - x')dt.$$

Note that the multiplicative noise term arising in Eq. (6) is perfectly uncorrelated in space, although it is not impossible that some spatial correlations arise from Eq. (6) as we will show later on. We also introduced the notation  $D = d\Delta x^2$ . We now see the connection between the local description of the random particle diffusion process with rate  $d$  [ $\text{s}^{-1}$ ] and the macroscopic diffusion coefficient  $D$  [ $\text{m}^2\text{s}^{-1}$ ].

Thanks to the system's linearity, it is possible to add back the deterministic advection flux:

$$d\eta(x, t) = [-\bar{u}_s\nabla\eta(x, t) + D\nabla^2\eta(x, t)] dt + [\lambda - (\sigma - \mu)\eta(x, t)] dt + \sqrt{2\mu\eta(x, t)} dW(x, t) \quad (7)$$

Here, it is possible here to make a parallel with point processes. Indeed, point processes are often defined by their rate function  $\eta(x, t)$  [*Cox and Isham*, 1980]. The simplest case is when the rate function is constant in time and space, resulting in a Poisson point process. When the rate function is a function of space and/or time, the process is called an inhomogeneous Poisson point process. Eventually, when the rate function is also a random variable, the process is called a doubly stochastic process, or Cox process [*Cox and Isham*, 1980]. This is the case with Eq. (7). To summarize, starting from a multivariate Markov process defined on lattice cells and described by a master equation, we end up with a model belonging to a general class of point processes, called doubly stochastic processes.

We now show how it is possible to simulate a probable realization of particle positions from Eq. (7). As noted earlier, by means of the Poisson representation,  $\eta(x, t)$  can be interpreted as the random rate of a Poisson distribution. First, we need to compute Eq. (7), to get a realization of  $\eta(x)$  at a given time  $t$ . This can be achieved using standard methods for stochastic differential equations (for instance an Euler-Maruyama scheme [*Kloeden and Platen*, 2011]). Once we get a realization of  $\eta(x)$ , we proceed as follows. We choose a constant  $C > \eta(x)$  and compute a realization of point positions according to a Poisson process with rate  $C$ . This can be achieved by taking the distance between points to be an exponentially distributed random variable with parameter  $1/C$ . We then randomly select or discard randomly point  $k$  according to the criteria:

if  $r < \eta(x_k)/C$ , keep point;  
if  $r > \eta(x_k)/C$ , delete point;

where  $r$  is drawn from a uniform distribution in  $[0, 1]$ . The remaining points form a possible observation of particle positions according to the model (Fig. 2).

In Fig. 2, it is possible to observe the clustering of particles around the region of high  $\eta(x)$  values, while for the Poisson process, particles positions are purely random so no clustering appears. The clustering of particles is a special feature of our model (when  $\mu > 0$ ) and can be quantified by the study of the second-order moments.

## 2.4. Moments

There exists a simple connection between moments of  $a$  in the Poisson representation and moments of the real variable  $N$ . Indeed, we can easily verify that the  $p$ -factorial moment of  $N$  is equal to the  $p$ -moment of  $a$

$$\begin{aligned} \langle n(n-1)\dots(n-p+1) \rangle &= \\ \sum_{n=0}^{\infty} n(n-1)\dots(n-p+1)P(n, t) &= \int a^p f(a) da \quad (8) \\ &= \langle a^p \rangle, \end{aligned}$$

which implies that  $\langle n \rangle = \langle a \rangle$  and  $\langle n^2 \rangle = \langle a^2 \rangle + \langle a \rangle$  [*Ancey and Heyman*, 2013]. We study the first and second-order moments of Eq. (7) below. As first-order moments have already been studied [*Ancey and Heyman*, 2013], we focus specially on second-order moments.

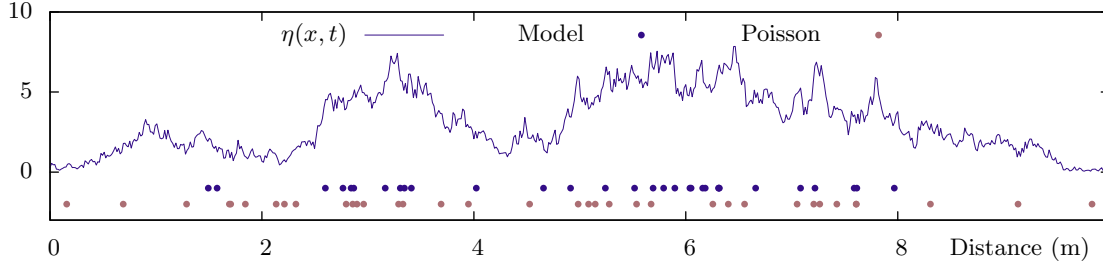


**Figure 2.** Example simulation of the rate process (Eq. (7)) and corresponding possible realization of particle positions. We also plot the Poissonian case (with the same mean rate) for comparison. Model parameters are  $\lambda = 0.05$  particles/m,  $\mu = 9.99 \text{ s}^{-1}$ ,  $\sigma = 10 \text{ s}^{-1}$ ,  $\bar{u}_s = 0.1 \text{ m s}^{-1}$  and  $D = 0.008 \text{ m}^2 \text{ s}^{-1}$

### 2.4.1. First-order moments

The average behavior of  $\eta(x, t)$  is easily obtained by dropping the noise term in Eq. (7). It is a linear advection-diffusion-reaction equation. In Appendix A, we show that it shares some similarities with the “BCRE” model of *Bouchaud et al.* [1995] which describes avalanches of dry granular matter. A stationary and homogeneous solution can be found provided that  $\sigma > \mu$ :

$$\langle \eta \rangle_s = \frac{\lambda}{\sigma - \mu}. \quad (9)$$

Given the relationships between the Poisson representation moments and the real variable moments (Eq. (8)), we have  $\langle \eta(x, t) \rangle = \langle \gamma(x, t) \rangle$  and thus  $\langle \gamma \rangle_s = \lambda/(\sigma - \mu)$ .

### 2.4.2. Second-order moments

#### 2.4.2.1. Spatial correlations

Let  $g(x, x', t)$  denote the spatial correlation function of the Poisson density variable  $\eta(x, t)$ . By definition we have:

$$\begin{aligned} g(x, x', t) &= \langle \eta(x, t) \eta(x', t) \rangle \\ &= \langle \eta(x, t) \eta(x', t) \rangle - \langle \eta(x, t) \rangle \langle \eta(x', t) \rangle. \end{aligned} \quad (10)$$

Taking the derivative of  $g$ :

$$\begin{aligned} dg(x, x', t) &= d \langle \eta(x, t) \eta(x', t) \rangle \\ &= \langle d\eta(x, t) \eta(x', t) \rangle + \langle \eta(x, t) d\eta(x', t) \rangle \\ &\quad + \langle d\eta(x, t) d\eta(x', t) \rangle. \end{aligned} \quad (11)$$

Note that  $d(\langle \eta(x, t) \rangle \langle \eta(x', t) \rangle)$  is zero by definition of the average. Using Itô’s approach to stochastic differential equations and Eq. (7), we get:

$$\begin{aligned} dg(x, x', t) &= D (\partial^2/\partial x^2 + \partial^2/\partial x'^2) \langle \eta(x, t) \eta(x', t) \rangle dt \\ &\quad - \bar{u}_s (\partial/\partial x + \partial/\partial x') \langle \eta(x, t) \eta(x', t) \rangle dt \\ &\quad + 2(\sigma - \mu) \langle \eta(x, t) \eta(x', t) \rangle dt + \langle \eta \rangle_s (2\lambda + \mu \delta(x - x')) dt \end{aligned} \quad (12)$$

In a spatially homogeneous situation,  $g(x, x', t)$  is a function of  $r = |x - x'|$  only, which we call  $g(r, t)$ . Thus, substituting Eq. (10) into Eq. (12), we obtain:

$$\frac{1}{2} \frac{\partial g(r, t)}{\partial t} = D \frac{\partial^2 g(r, t)}{\partial r^2} - (\sigma - \mu) g(r, t) + \mu \langle \gamma \rangle_s \delta(r) \quad (13)$$

Note that the advection term disappears because  $\partial/\partial x = -\partial/\partial x'$ . Thus, the spatial correlation has no dependence on the mean velocity of particles. For  $t \rightarrow \infty$ , the stationary solution  $g_s(x)$  is obtained by means of Fourier transforms (see Appendix B).

The relation between second-order moments in the Poisson representation and in the real variable is obtained using

Eq. (8). In our case, this yields the simple relation:

$$\langle \eta(x, t) \eta(x', t) \rangle = \langle \gamma(x, t) \gamma(x', t) \rangle - \delta(x - x') \langle \gamma(x, t) \rangle.$$

Thus, the stationary homogeneous spatial correlation function of the particle activity reads:

$$\begin{aligned} \langle \gamma(x, t) \gamma(x', t) \rangle_s &= \delta(x - x') \langle \gamma \rangle_s \\ &\quad + \frac{\langle \gamma \rangle_s \mu}{2\ell_c \sigma - \mu} \exp\left(-\frac{|x - x'|}{\ell_c}\right), \end{aligned} \quad (14)$$

where we have introduced the correlation length in the  $x$ -direction  $\ell_c = \sqrt{D}/(\sigma - \mu)$ . The stationary spatial correlation function is thus the sum of a Dirac delta function of intensity equal to the mean density of moving particles and a term corresponding to non-Poissonian behavior. The latter has a characteristic length scale defined by  $\ell_c$ . Thus, the correlation length increases with the diffusivity of particles and the collective entrainment rate, but decreases with the deposition rate.

The correlation length becomes infinitely large when  $\mu \rightarrow \sigma$ . When  $\mu = \sigma$ , the system loses its stability and we observe an exponential increase in the number of moving particles. This limit might be associated with a phase transition. Physically, deposition dissipates energy and counterbalances collective entrainment.

Another quantity of interest, often used to describe a spatial point process, is the conditional intensity  $h(x - x')$ , that gives the conditional probability of finding a particle at  $x'$  given that there is a particle at  $x$  [*Cox and Isham*, 1980]. The conditional intensity and the correlation function are directly related by:

$$\langle \gamma(x, t) \gamma(x', t) \rangle_s = \delta(x - x') \langle \gamma \rangle_s + \langle \gamma \rangle_s h(x - x') - \langle \gamma \rangle_s^2,$$

so that by identification, we have :

$$h(x - x') = \langle \gamma \rangle_s + \frac{1}{2\ell_c} \frac{\mu}{\sigma - \mu} \exp\left(-\frac{|x - x'|}{\ell_c}\right). \quad (15)$$

A more convenient function for data analysis is the  $K$ -function [*Ripley*, 1976], where  $K(x)$  represents the expected number of moving particles found in a ball of radius  $x$  centered on a particle location divided by the mean process rate. This can be calculated from the conditional intensity function by:

$$\begin{aligned} K(x) &= \frac{1}{\langle \gamma \rangle_s} \int_0^x h(u) du \\ &= x + \frac{1}{\langle \gamma \rangle_s} \frac{\mu}{\sigma - \mu} \left[ 1 - \exp\left(-\frac{x}{\ell_c}\right) \right]. \end{aligned} \quad (16)$$

For a Poisson point process in one dimension, we have  $K(x) = x$ . Furthermore, Eq. (16) shows that  $K(x) > x$

if  $\mu > 0$ ; so the point process is said to be clustered. This is not surprising as we observed a clustering of particles in Fig. 2.

#### 2.4.2.2. Spatio-temporal correlations

We are now interested in the spatio-temporal correlation function of Eq. (7). Following *Chaturvedi and Gardiner* [1978], we define:

$$G(x, t) = \langle \gamma(x, t), \gamma(0, 0) \rangle_s \quad (17)$$

For any linear Markovian system, a linear equation also exists for the evolution of the time correlation [Gillespie, 1991]:

$$\frac{\partial G(x, t)}{\partial t} = D \frac{\partial^2 G(x, t)}{\partial x^2} - \bar{u}_s \frac{\partial G(x, t)}{\partial x} - (\sigma - \mu) G(x, t) \quad (18)$$

with the initial condition  $G(x, 0)$  given by Eq. (14). By making the transformations  $\tilde{t} = (\sigma - \mu)t$ ,  $\tilde{x} = x/\ell_c$ , we can obtain the expression of the spatio-temporal correlation function (details in Appendix C) that is

$$G(\tilde{x}, \tilde{t}) = G_d(\tilde{x}, \tilde{t}) + G_r(\tilde{x}, \tilde{t}) \quad (19)$$

with

$$G_d(\tilde{x}, \tilde{t}) = \frac{\langle \gamma \rangle_s}{2\ell_c \sqrt{\pi \tilde{t}}} \exp \left[ -(\tilde{x} - \text{Pe} \tilde{t})^2 / \tilde{t} - \tilde{t} \right] \quad (20)$$

and

$$G_r(\tilde{x}, \tilde{t}) = \frac{\langle \gamma \rangle_s}{4\ell_c} \frac{\mu}{\sigma - \mu} \cdot \left\{ \exp \left[ \tilde{x} - \text{Pe} \tilde{t} \right] \text{erfc} \left[ (1 + \text{Pe}/2) \sqrt{\tilde{t}} + \tilde{x}/(2\sqrt{\tilde{t}}) \right] + \exp \left[ \text{Pe} \tilde{t} - \tilde{x} \right] \text{erfc} \left[ (1 + \text{Pe}/2) \sqrt{\tilde{t}} - \tilde{x}/(2\sqrt{\tilde{t}}) \right] \right\}. \quad (21)$$

$\text{Pe} = \bar{u}_s \ell_c / D$  can be interpreted as a local Péclet number comparing the relative importance of the mean advection against the diffusion process over the correlation scale  $\ell_c$ .  $G(x, t)$  is the sum of two contributing terms.  $G_d(x, t)$  quantifies the spread and advection of the delta-correlated Poissonian term of Eq. (14) while  $G_r(x, t)$  encodes the relaxation of the non-Poissonian correlations through time. If  $\mu = 0$ , fluctuations are purely Poissonian so that  $G_r(x, t) = 0$ . In Fig. 5, we plot  $G(\tilde{x}, \tilde{t}) / (\langle \gamma \rangle_s / \ell_c)$  for different values of  $\text{Pe}$ .

### 3. Local and global fluctuations

After deriving spatial and spatio-temporal correlation functions, we examine how they can be used to characterize fluctuations in the particle activity. Specifically, we want to determine the relative importance of these fluctuations compared to the mean activity, depending on the spatial or temporal scales considered.

#### 3.1. Spatial fluctuations

Let us consider the number of moving particles in a window of length  $L$  at a given time  $t$ :

$$N(L, t) = \int_L \gamma(x, t) dx. \quad (22)$$

The volume average of this number is:

$$\text{Mean}[N(L, t)] = \left\langle \int_L \gamma(x, t) dx \right\rangle = \langle \gamma \rangle_s L, \quad (23)$$

while the expected variance of this number, also called the variance of the sample mean, is defined by:

$$\text{Var}[N(L, t)] = \int_L \int_L \langle \gamma(x, t), \gamma(x', t) \rangle dx dx'. \quad (24)$$

Introducing Eq. (14) into Eq. (24) and integrating it (see Appendix D), we find:

$$\text{Var}[N(L, t)] = \langle \gamma \rangle_s L + \langle \gamma \rangle_s \ell_c \frac{\mu}{\sigma - \mu} \left( L/\ell_c + e^{-L/\ell_c} - 1 \right). \quad (25)$$

Eq. (25) shows the dependence of the variance of  $N(L, t)$  on the length  $L$  of the sampling window. Let us define the dispersion index  $I(L)$  as the ratio of the variance over the mean:

$$I(\tilde{L}) = \frac{\text{Var}[N(\tilde{L}, t)]}{\text{Mean}[N(\tilde{L}, t)]} = 1 + \frac{\mu}{\sigma - \mu} \left( 1 + \frac{e^{-\tilde{L}} - 1}{\tilde{L}} \right), \quad (26)$$

with  $\tilde{L} = L/\ell_c$ .

The dispersion index is used to characterize the relative positions of points (particles locations). Three classes are generally distinguished depending on the value of  $I$ : under-dispersed processes for  $I < 1$ ; purely random processes (or Poisson process) when  $I = 1$ ; and over-dispersed or clustered processes when  $I > 1$  (Fig. 3).

In our model, the dispersion index is shown to grow from 1, when the window is small, to the constant value  $1 + \mu/(\sigma - \mu)$ , as the window length tends to infinity (Fig. 4). In other words, depending on the length of observation, the process exhibits a different statistical behavior.

The limit to the Poisson process ( $I = 1$ ) when  $L \rightarrow 0$  is explained by the presence of the Dirac delta function in the

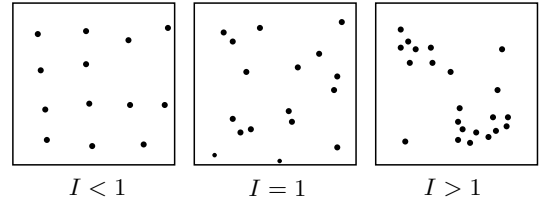


**Figure 3.** Example of a realization of point positions in a two-dimensional space depending on the value of  $I(L)$ . Here,  $L$  can be interpreted as the length of the box.

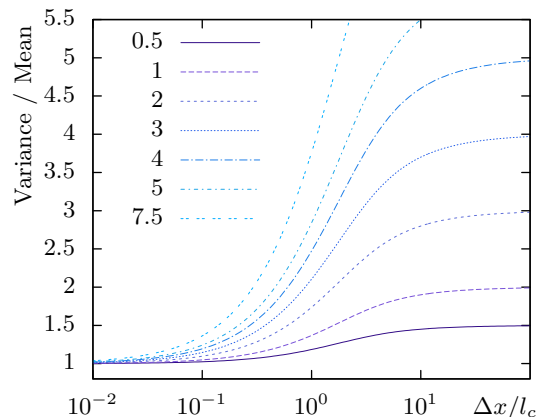


**Figure 4.** Eq. (26) for different  $\mu/(\sigma - \mu)$  values.

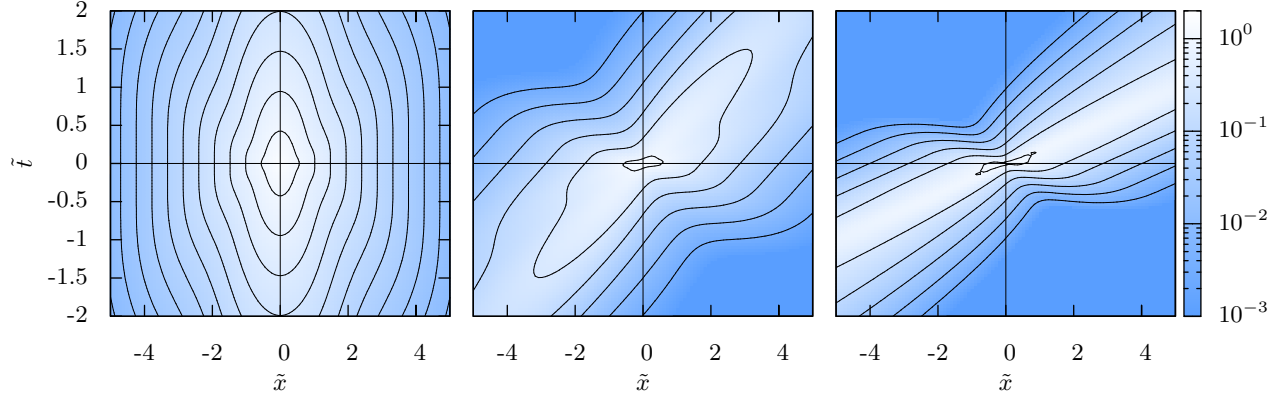


**Figure 5.** Contour plot of  $G(\tilde{x}, \tilde{t}) / \langle \gamma \rangle_s / \ell_c$  for  $Pe = 0, 2$  and  $5$  (from left to right) taking  $\mu = 3.5 \text{ s}^{-1}$  and  $\sigma = 4.0 \text{ s}^{-1}$ .

spatial covariance (14). For decreasing values of  $L$ , a limit will be reached when most of the the sampling windows usually contain no particles, or rarely one particle. This limiting behavior can be seen as a Bernoulli process; that is, within the limit of small probability of occurrence, a Poisson process.

On the contrary, when  $L \rightarrow \infty$ ,  $I$  reaches a constant value  $I(\infty)$ . Note that  $I(\infty) > 1$  if  $\mu > 0$ . Moving particles are thus expected to form clusters during their motion when collective entrainment is considered.

### 3.2. Temporal fluctuations

Most of bedload measurement devices do not sample bedload spatially but temporally [Bunte and Abt, 2005]. For instance, weighting bins [Singh et al., 2009] or geophone sensors [Rickenmann et al., 2012] monitor the bedload discharge at a given location over time. In this case, Eq. (26) cannot be used to test stochastic predictions. Instead, we have to look for the fluctuations of the mean number of particles that pass through a given location during a time of length  $T$ :

$$N(x, T) = \int_T \gamma(x, t) dt.$$

The variance of this number is defined by:

$$\begin{aligned} \text{Var}[N(x, T)] &= \int_T \int_T \langle \gamma(x, t), \gamma(x, t') \rangle dt dt', \\ &= \int_T \int_T G(0, t - t') dt dt'. \end{aligned} \quad (27)$$

Unfortunately, this integral is too complex to be calculated analytically but estimates can readily be obtained at large  $Pe$  (for high average particle velocity). In this case, it can be assumed that the spatial correlation function is projected on the temporal axis without deformations. The equivalence between time and space is then given by  $t \sim x/\bar{u}_s$ . This approximation can be compared to Taylor's frozen-flow hypothesis in turbulent flows with a dominant average velocity. In other words, the relative positions of particles in space correspond exactly (up to a scaling factor) to their relative time of passage through a given location. From Eq. (26), this approximation leads to:

$$I(\tilde{T}) = \frac{\text{Var}[N(x, \tilde{T})]}{\text{Mean}[N(x, \tilde{T})]} = 1 + \frac{\mu}{\sigma - \mu} \left( 1 + \frac{e^{-\tilde{T}} - 1}{\tilde{T}} \right), \quad (28)$$

with  $\tilde{T} = T/t_c$ . We introduced  $t_c = \ell_c/\bar{u}_s$  as the characteristic time that is related to the frozen-flow hypothesis. Thus, at the high particle velocity limit, the variance of the sampled solid discharge at a given location has the same dependence on the acquisition duration as the variance of the number of moving particles has on the observation window length. We demonstrate below that Taylor's frozen-flow hypothesis, often used in fluid turbulence, is irrelevant for bedload transport.

### 3.3. Consequences for model fitting

Eq. (26) and (28) have major consequences for parameter fitting. Consider a sample of particles trajectories observed in a window of length  $L$ . If  $L \ll \ell_c$ , the experimental variance of the number of moving particles is likely to be close to the arithmetic mean so that, one can naturally conclude in favor of a Poisson distributed variable. However, this is obviously wrong if  $\mu > 0$ . If  $L \sim \ell_c$ , the observed variance will be greater than the mean, and we can now exclude the Poisson distribution. However, by changing  $L$  a little, the dispersion index also changes, such that it is not possible to find a unique set of model parameters (with the method of moments, for instance) that works at all scales. The larger the window, the larger the index and the larger the fluctuations around the mean. Finally, if  $L \gg \ell_c$ , the index eventually reaches a plateau. For these observation windows, it is possible to fit a single set of parameters that is valid at both small and large scales. The same argument applies for the sampling of particles over time in the frozen-flow hypothesis. We will show below that the minimum length  $L$  required is often so large that the majority of experiments cannot ensure an unbiased estimation of the parameters. Worse, bias always leads to the under-estimation of large scale particle activity fluctuations. This is partly the topic of the next section, where we present three different experimental data sets.

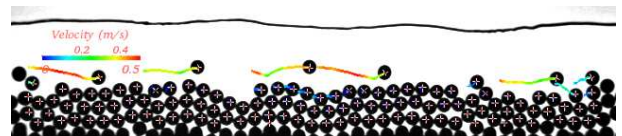


**Figure 6.** Image recorded during a B experiment and visualization of particles trajectories after image processing.

**Table 1.** Experimental parameters and model fits.

	$d_{50}$	$\tau_s$	Fr	$\tan\theta$	$\bar{u}$	$\bar{h}$	$q_s$	$\langle\gamma\rangle_s$	$u_s$	$D$	$\lambda$	$\sigma$	$\mu$	$\ell_c$	Pe	$I(\infty)$
B12-9	6	0.10	2.20	12.5	0.42	0.7	9.3	63.0	0.12	25	86.4	8.42	7.05	4.27	2.05	6.15
B10-6	6	0.11	1.42	10.0	0.41	1.0	5.3	28.9	0.16	27	41.8	6.50	5.05	4.32	2.63	4.48
B10-7	6	0.12	1.37	10.0	0.41	1.1	6.7	32.3	0.19	25	54.4	5.58	3.90	3.85	2.98	3.32
B10-8	6	0.13	1.38	10.0	0.44	1.2	8.0	37.1	0.18	33	65.4	6.46	4.70	4.33	2.35	3.67
B10-9	6	0.14	1.36	10.0	0.44	1.3	10.0	43.4	0.18	33	66.3	5.38	3.85	4.65	2.49	3.51
B10-16	6	0.19	1.24	10.0	0.48	1.7	15.4	69.3	0.19	43	159.6	6.70	4.40	4.32	1.90	2.91
B7-9	6	0.21	1.15	7.5	0.56	2.5	8.7	37.7	0.21	30	54.6	5.45	4.00	4.55	3.22	3.75
R0-1	0.5	0.06	0.35	$\ll 1$	0.31*	12.5	78.9	1711	0.05	1.3	85.5	2.51	2.46	5.16	17.88	50.20
H4-2	8	0.11	1.35	4.14	0.78	3.4	1.6	5.9	0.27	35	24.8	0.58	0.43	15.3	12.04	3.87
H2-2	8	0.07	1.24	2.43	0.76	3.8	2.3	8.5	0.27	30	37.1	0.40	0.25	14.1	12.50	2.67

$d_{50}$ , mean particle diameter [mm];  $\tau_s$ , Shields stress [-]; Fr, Froude number [-];  $\tan(\theta)$ , slope angle [%];  $\bar{u}$ , mean fluid velocity [m/s];  $\bar{h}$ , mean water depth [cm];  $q_s$ , mean output solid discharge [particles/s],  $\langle\gamma\rangle_s$  mean activity [particles/m].  $u_s$  mean particle velocity [m/s],  $D$  diffusion coefficient [cm<sup>2</sup>/s],  $\lambda$  entrainment rate [particles/m/s],  $\sigma$  deposition rate [s<sup>-1</sup>],  $\mu$  collective entrainment rate [s<sup>-1</sup>],  $\ell_c$  correlation length [cm], Pe local Péclet number [-],  $I(\infty)$  dispersion index for an infinite window length [-]. \*: In this experiment,  $\bar{u}$  is the average fluid velocity 1 cm above the bed.

## 4. Experiments

To test our previous theoretical predictions, we used three different experimental data sets. Two of them have been previously published [Ancey *et al.*, 2008; Roseberry *et al.*, 2012]. The third comes from an experimental setup especially built to observe spatial and temporal fluctuations of bedload at the same time. All three studies provide high resolution measurements of particle transport using high speed imaging.

Hereafter, we denote all Böhm *et al.* [2004] experiments by using the prefix B, the new data set using H and Roseberry *et al.* [2012] experiment using R. The numbers following the prefix specify experimental slope and solid discharge. For instance B12-9 stands for Böhm *et al.* [2004] experiment conducted using a 12% sloping flume with a mean solid discharge of 9 particles/s.

### 4.1. Experimental setups.

#### 4.1.1. B experiments.

These experiments were carried out in a narrow steep flume where sediment consisted of glass beads of equal size (6 mm). Particle transport was completely two-dimensional;

this allowed Böhm *et al.* [2004] to take pictures through the side wall and detect and track individual particles via image processing. Camera resolution was  $640 \times 192$  pixels with a frame rate of 129.2 frame per seconds (fps). Each sequence comprised 8000 images corresponding to a duration of approximately 1 min. The acquisition length was 22.5 cm, for a resolution of 0.3 mm/pixel. Thus this imaging technique covers about 2 orders of magnitude in space. For further information on the experimental conditions, the reader is referred to [Böhm *et al.*, 2004; Ancey *et al.*, 2006, 2008].

Fig. 6 shows an example of a recorded image and the corresponding reconstruction of particle positions and velocities using image processing.

#### 4.1.2. R experiment.

Roseberry *et al.* [2012] presented a set of experiments where particle trajectories were sampled in a two-dimensional window of the bed viewed from the top. High-speed imaging at 250 fps over a 7.57 cm (streamwise) by 6.05 cm (cross-stream) bed-surface domain, and with  $1280 \times 1024$  pixels resolution provided the basis for tracking particle motions (with a precision of 0.06 mm/pixel). Bed material consisted of relatively uniform coarse sand with an average diameter of  $d_{50} = 0.5$  mm.

The data set involved one experiment with a total duration of 0.4 seconds, i.e. 100 frames (Fig. 7). In contrast with the two other data sets, the R experiment concerns relatively small particles (sand) over shallow slope (the slope is not given in [Roseberry *et al.*, 2012] but one can guess it because the Froude number is much lower than unity). We will show that the same spatial patterns form in their experiments.

#### 4.1.3. H experiments.

The originality of this data set compared to the two others lies in its high temporal and spatial resolutions. The length of the observation window was slightly less than 1 m (with a precision of about 1 mm/pixel) while the duration of a sequence was 10 seconds.

Experiments were carried out in a 2.5-m-long flume. The erodible bed was made of natural sediment particles with mean diameter of 8mm. The flume was 3.5 cm wide and the water depth was about 3.7 cm during experiments. The channel slope ranged between 2.4% and 4%. The flow was fully supercritical. As the flow depth to channel width ratio was relatively large, any three dimensional variation of the bed surface was avoided. The channel bed remained nearly flat during the whole experiment, so that an approximation of homogeneous transport conditions could be made.

The image sequences were taken by two cameras placed side by side so that their field of vision overlapped by a few centimetres. Located in the central part of the flume, they filmed through the transparent side wall. Camera resolution was  $1024 \times 200$  pixels while the frame rate was set to 150 fps.

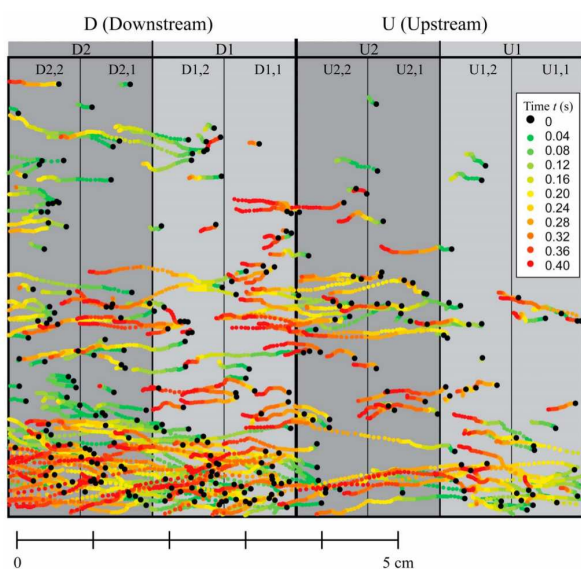


**Figure 7.** Map view of R experiments showing particle motions occurring during the 0.4 sec time series; note the clustering of motions, partly reflecting effects of the turbulent sweeps. (Reproduced from [Roseberry *et al.*, 2012] with the authorization of the authors and AGU.)

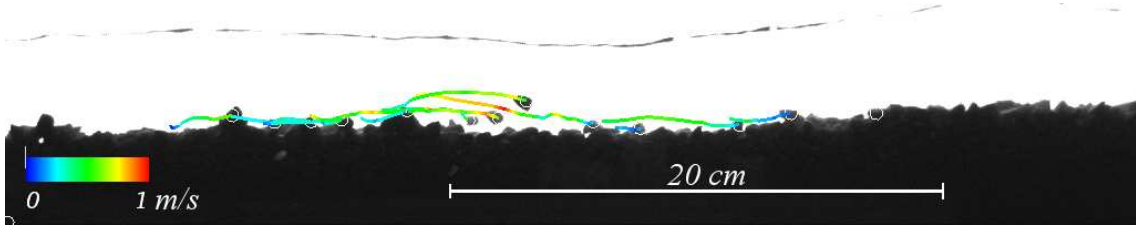


Figure 8. Preview of particle trajectories obtained from the first camera in the H experiments.

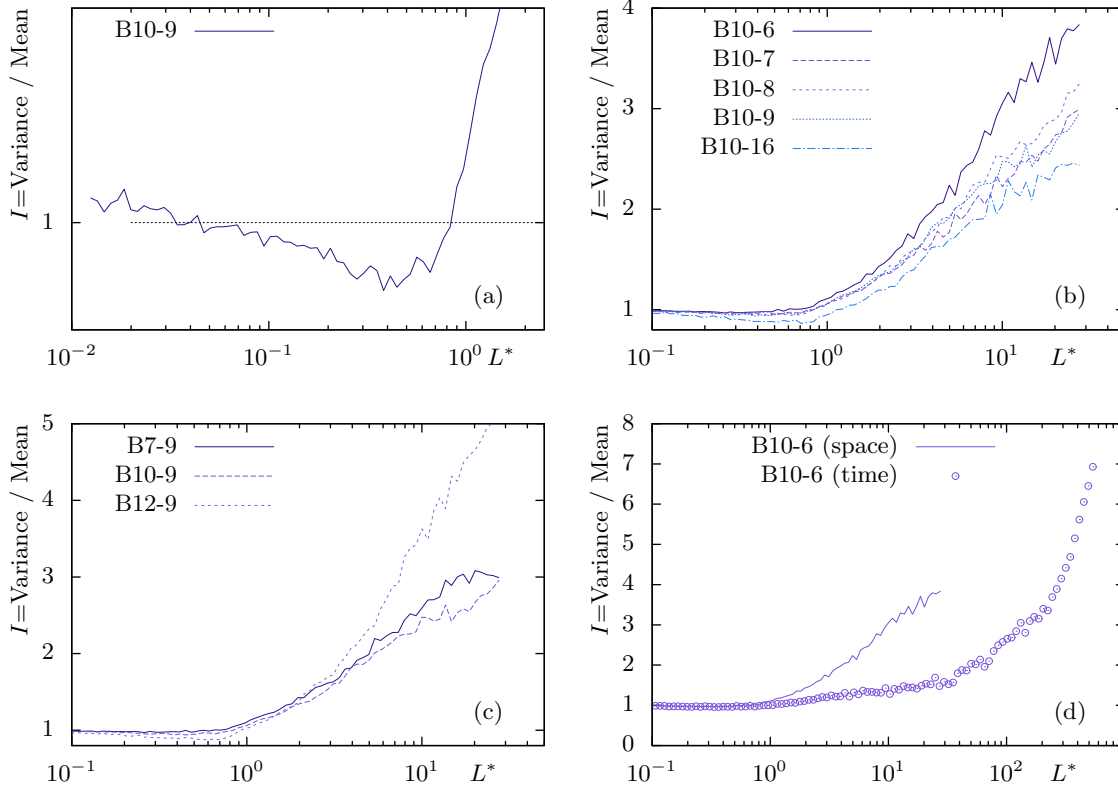


Figure 9. Dispersion indices through different scales for the B experiments.  $L^* = L/d_{50} = \bar{u}_s T/d_{50}$ .

Given the memory limitation during acquisition, sequences of 10 seconds (1500 images) were taken repeatedly.

Image processing and automatic particle tracking were then performed on these images. Systematic human monitoring was applied to make sure that the automatic-capture algorithm was not missing any particles. The processing steps from the raw images to particles trajectories were the following:

1. First we treated the raw images using the powerful yet simple method of median background subtraction [Yilmaz *et al.*, 2006]. This allows a distinction between an immobile background (made up of particle resting on the bed) and a moving foreground (the moving particles).
2. A tracking algorithm was then used to detect and follow the moving particles in the foreground images. We used *polyparticletracker* [Rogers *et al.*, 2007], a powerful algorithm that is able to track particles of various shapes. At this stage, about 70 % of the particle trajectories had been correctly reconstructed.
3. Finally, we performed a manual check to track the particles that the algorithm had missed. This was done using ImageJ software and the MtrackJ plugin.

This was the most time consuming task (approximately 3 hours for 10 seconds of film), thus only two experiments at different flume angles are presented here. Each experiment represents 100 seconds of acquisition, for about 2000 particles trajectories. We have summarized the experimental characteristics in Tab. 1.

## 4.2. Experimental results

### 4.2.1. B experiments

In accordance with *Ancey et al.* [2008], we included both rolling and saltating particles in the group of moving particles. A velocity threshold was used to discriminate between resting or moving particles. It was not always clear which threshold to apply, as a moving particle can have its instantaneous velocity equal to zero (but a non-zero acceleration). To avoid this, we applied a threshold of 0.05 m/s on a time moving average of the velocities over about 5 frames (i.e.  $\sim 0.04$ s).

The experimental dispersion indices are presented in Fig. 9 (see Appendix E for the computation details). Note that the correlation length is not known *a priori* and thus we scale the space axis by the diameter  $d_{50}$  of the particle:  $L^* = L/0.006$ .

As expected, the dispersion index changes through spatial scales. From a Poisson type process (the mean equals the variance) at small scales ( $L^* \rightarrow 0$ ),  $I(L^*)$  continuously increases with increasing scales (see Fig. 9(b),(c) and (d)).

One striking feature of the experimental dispersion index is the slight decrease below unity for  $L^* \sim 1$  (Fig. 9(a)). This phenomenon results from negative values in the correlation function at those scales and cannot be described by our Markov model. Indeed the theoretical correlation function (Eq. (14)) is strictly greater than zero so that the variance is expected to grow monotonically. The presence of negative values in the experimental correlation function is explained by the finite diameter of the particles. Thus, there is less probability of finding two particles separated by a distance smaller than the particles' diameters. Note that we use the term “less probability” and not “zero probability” because the moving particles in an observation window are summed over the whole water depth ( $z$  direction), so that it is still possible that the distance separating two moving particles (in the  $x$  direction) is less than the particle diameter. This results in anti-correlation at scales close to the particle diameter ( $L^* \sim 1$ ).

For a constant flume angle (10%), the variance of experiments carried out at different Shields stresses (at different transport stages) is represented in Fig. 9(b). It is unclear how changes in the Shields stress affect the experimental curve since all of the curves roughly superimpose one another. Recall that the theoretical expression (26) depends only on the collective entrainment rate  $\mu$  and deposition rate  $\sigma$ . The latter is a function of the particle fall velocity while the former has been reported not to change much with fluid forcing [Ancey *et al.*, 2008; Heyman *et al.*, 2013]. In all these experiments, the only parameters that change significantly are the fluid entrainment rate  $\lambda$  and the average particle velocity  $\bar{u}_s$ . Because the dispersion index does not depend on these variables, we expect all curves to overlap.

In Fig. 9(c), we plot the dispersion indices of experiments carried out at different flume angles but with the same solid discharge. Generally, it can be seen that experiments carried out at steeper angles show a larger dispersion index at large scales than those conducted at shallower angle. This is true for B12-9, whose variance reaches five times the mean, whilst experiments B7-9 and B10-9 show fluctuations only equal to about three times the mean. This indicates that the ratio  $\mu/(\sigma - \mu)$  may increase with slope angle.

The relatively high temporal resolution (30 seconds for each experiment) allowed us to test the frozen-flow hypothesis against experimental data. To that end, we randomly chose a set  $x_i$  of locations over the maximum observation

length. We then counted the moving particles that crossed these locations. The variance of the counts as a function of the counting duration is then computed. As explained previously, the frozen-flow hypothesis states that spatial correlations are identically transformed into temporal correlations with the relation  $x \sim \bar{u}_s t$ . Spatial and temporal dispersion indices should thus fall on the same curve with the appropriate scaling of the time axis (see Fig. 9(d)). In a similar way to the spatial dispersion index, the temporal index increases from unity at the smallest time scales to larger values at longer time scales. However, we can infer from Fig. 9(d) that the frozen-flow hypothesis is far from being correct for the B experiments—the spatial and temporal indices are extremely different. Indeed, we will show below that the local Péclet number of those experiments lies between 2 and 3, showing that the mean advection is not the only dominant term in the spatio-temporal correlation function.

#### 4.2.2. R experiments

As the R experiment was originally two dimensional, we first summed the number of moving particles over the window width. Then the procedure described in Appendix E was applied to compute the dispersion index. Again, the index curve is seen to increase through spatial scales (Fig. 10). From a Poisson type process (the mean equals the variance) at small scales, the index continuously rises with increasing scales. Note that, as for the B experiments, the plateau is not reached when the scale tends to the maximum observable length.

Interestingly enough, we see that spatial correlations occur even for gently sloping bed under subcritical flow conditions. Recall that collective entrainment is the only cause of spatial correlation in our model. In this case, for small particle diameters and gentle slopes, collective entrainment is likely to be triggered by coherent turbulent structures rather than by direct particle-particle interaction (for a discussion about the possible causes of collective entrainment, see [Heyman *et al.*, 2013]).

Another noteworthy feature is the relative magnitude of the fluctuations: up to 20 times the mean particle activity. Although the B experiments were carried out on a steeper bed, their fluctuations did not exceed 5 times the mean particle activity. A reasonable explanation might be that particle diameters in the R experiment were much smaller than in the B experiments. As a consequence, turbulent eddies may entrained many more particles at the same time, thus making the collective effects appear stronger.

#### 4.2.3. H experiments

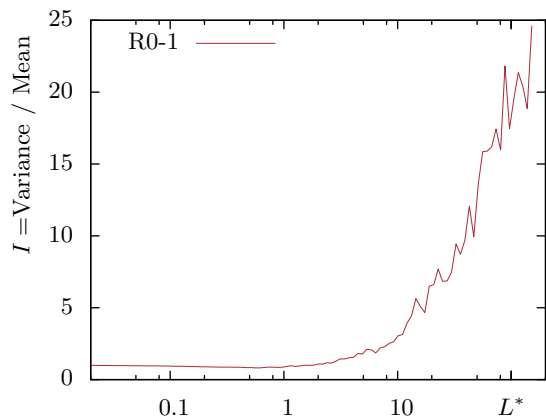
The dispersion indices of these experiments developed in a similar way to those of the two preceding experiments (Fig. 11(b)). Despite the relatively large observation window, the plateau was not reached. Similarly to Ancey *et al.* [2008] experiments, the steepest sloped experiment –H4-2– had a larger index than H2-2. This substantiates the idea that  $\mu/(\sigma - \mu)$  increases with slope.

Fig. 11(a) also shows the comparison between spatial and temporal averages. As expected, the agreement was perfect, such that it was equivalent to computing the average particle activity in time or in space. This was not true for the second-order moments (Fig. 11(b)). Still, the agreement between the two curves was better than for the B experiments but a perfect overlap was not obtained. Below, we show that the local Péclet number is about 12, a value still too small to ensure the relevance of the frozen-flow hypothesis.

### 4.3. Model calibration

In this section, we show how it is possible to determine the model parameters ( $\lambda, \mu, \sigma, V, D$ ) from each experimental data set.

The mean velocity is the easiest parameter to compute; it is the average of the velocities of all moving particles over all trajectories (Fig. 12(a)).



**Figure 10.** Spatial dispersion index for the R experiment.  $L^* = L/d_{50}$ .

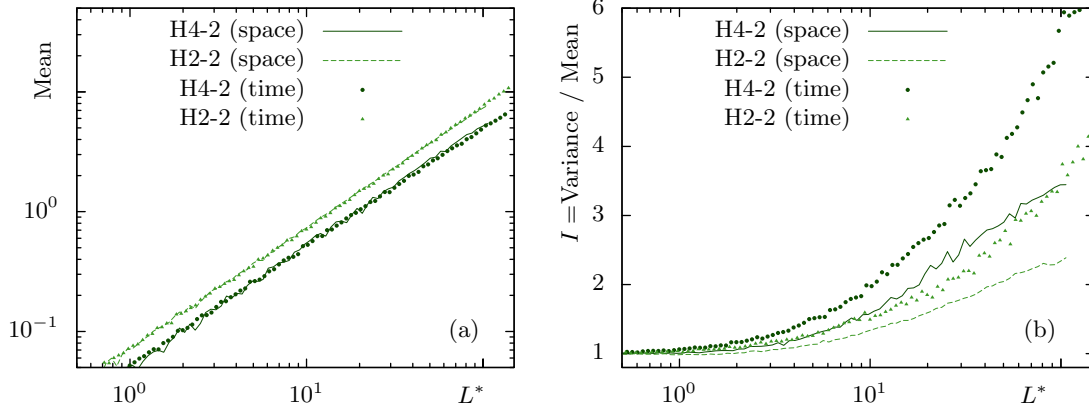


**Figure 11.** H experiments. (a) Comparison between the sample mean of moving particles computed in space and in time. (b) Comparison between the dispersion index computed in space and in time.  $L^* = L/d_{50} = \bar{u}_s T/d_{50}$ .

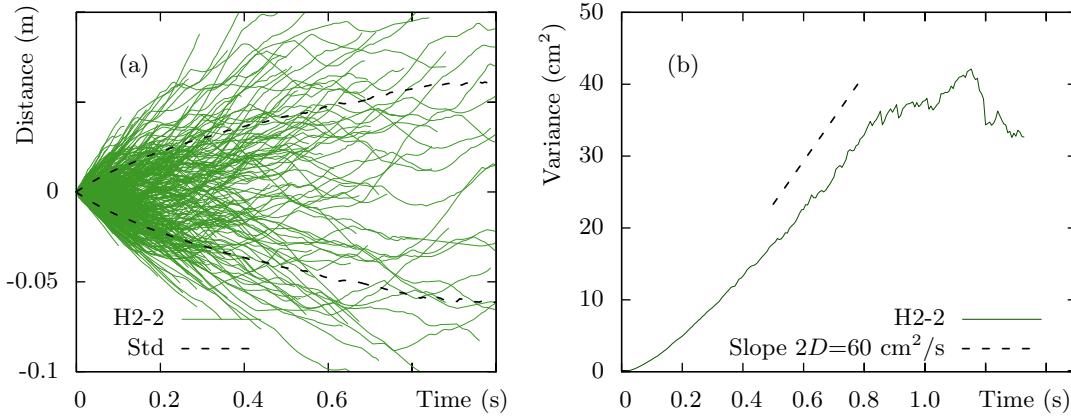


**Figure 12.** (a) A few particles trajectories (the mean displacement computed from the mean particle velocity  $\bar{u}_s$  is subtracted from each trajectories). (b) Mean squared displacement of moving particles through time.

Diffusivity is harder to estimate. Unlike the movement of Brownian particles that undergo uncorrelated motion, the velocities of bedload particles shows some non-vanishing correlation over time (Fig. 12(a)). Moreover, as particles start from rest and eventually return to rest after some time, the velocity of a single particle exhibits periodicity. According to *Furbish et al.* [2012b], the effective diffusivity can be obtained by calculating the variance of the particle velocity as well as the integral of its auto-correlation. However, because of the periodicity, the integral does not grow monotonically towards a constant value over long time scales. Thus, we use a different method here. The mean squared displacement of a particle undergoing diffusion is known to evolve linearly with time  $\langle X^2 \rangle \propto 2Dt$  [*Taylor, 1922*]. Finding  $D$  is thus equivalent to fitting the particle's mean squared displacement through time with a linear regression curve (Fig. 12(b)). For short time scales ( $t < 0.2\text{s}$ ), the mean squared displacement shows a  $t^2$  dependence, confirming the super-diffusive behavior due to particle velocity correlations. A linear dependence on time is seen to occur between about 0.5 and 0.8 s. For times longer than 0.8 s, there are not enough sufficiently long trajectories to get an accurate estimate of  $\langle X^2 \rangle$ . For each experiment, we thus calculate  $D$  by fitting a linear curve on the time range  $t = [0.5, 0.8]$  s.

The mean deposition rate is readily obtained using individual particle trajectories. To find  $\sigma$ , we construct a list of the deposition event times. The time series forms a counting

process whose mean rate, divided by the mean number of moving particles, is equal to  $\sigma$ .

The main difficulties lie in the determination of the fluid entrainment rate  $\lambda$  and the collective entrainment rate  $\mu$ . Indeed, it is impossible to distinguish between the two by looking at single particle trajectories. Moreover, the two processes are likely to act in a coupled way: a turbulent event occurring along with a particle impact has a greater chance of entraining an immobile particle than if both happened individually. We thus need to consider the model's prediction to determine their relative importance. Note that if one of them is known, the second is directly determined by the steady-state mean  $\langle \gamma \rangle_s = \lambda/(\sigma - \mu)$ . Our model thus requires a single tuned parameter. To find  $\mu$  (or equivalently  $\lambda$ ), one needs to calculate the limiting value of the spatial dispersion index  $I(\infty)$  for a long enough observation window (for  $L = 100\ell_c$ , the dispersion index equals approximately 99% of its infinite value). From Eq. (26), we get:

$$\begin{aligned} \mu &= (1 - I(\infty)) \sigma \\ \lambda &= \langle \gamma \rangle_s (\sigma - \mu) \end{aligned} \quad (29)$$

Unfortunately,  $I(\infty)$  is not known in the experiments presented here, as the dispersion index did not reach a constant value for the maximum available window length. We must

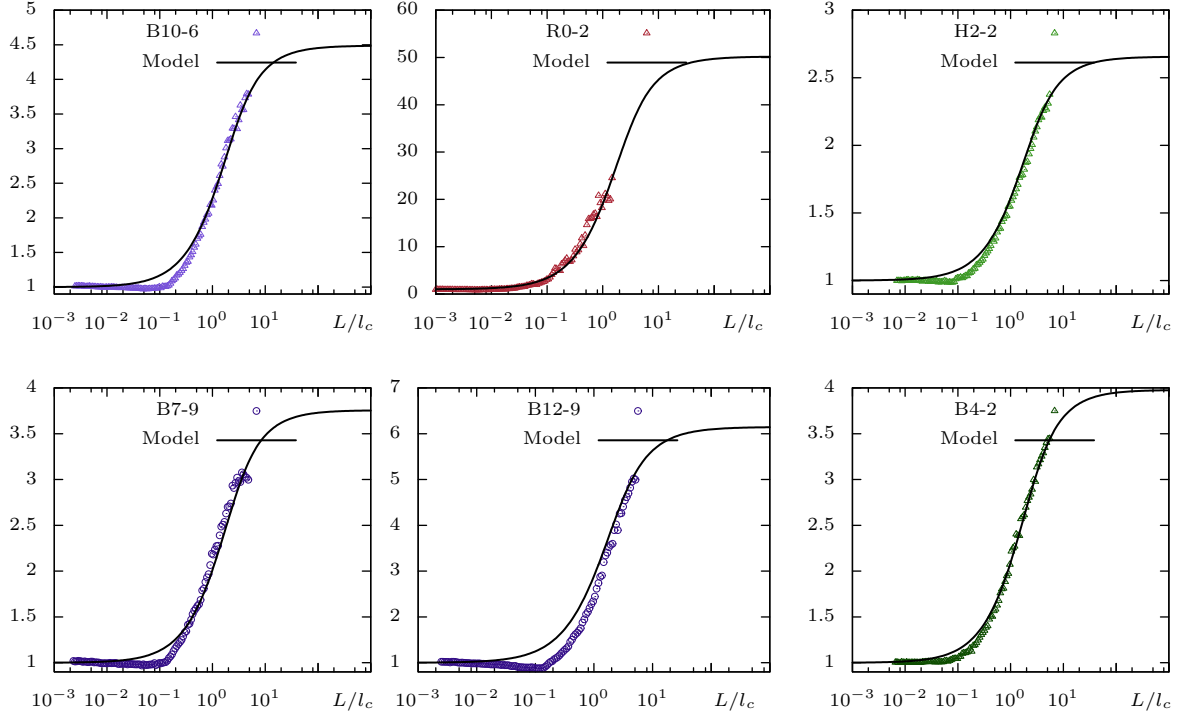


**Figure 13.** Experimental dispersion indices and theoretical predictions from Eq. (26). Note that the  $x$ -axis is scaled by the correlation length  $\ell_c$ .

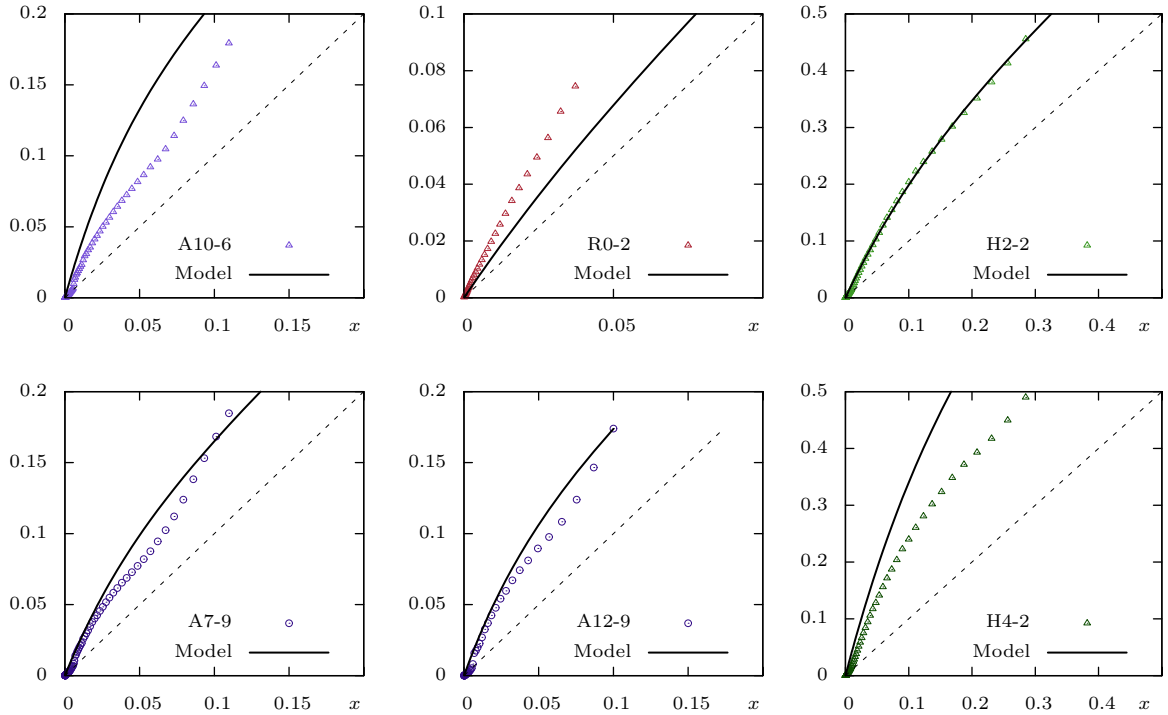


**Figure 14.** Experimental K-function (dots) and comparison with theoretical predictions (line). The Poissonian case is also represented by dashed lines.

thus attempt to approach the experimental index curve by tuning parameter  $\mu$ . Fig. 13 shows an example, where experiments are compared to the theoretical predictions. The

agreement between theory and experiment is good and the growth rate of the index curves is accurately reproduced. A summary of the calibrated parameters for all the experiments are given in Tab. 1. We also compare the experimen-

tal  $K$ -function to its theoretical expression (16) in Fig. 14. The agreement between theory and experiments is not as good for the  $K$ -function as for the dispersion index. This can be explained by the fact that the value of  $\langle \gamma \rangle_s$  appears in Eq. (16) whilst it is absent from Eq. (26). Meanwhile, estimation of  $\langle \gamma \rangle_s$  needs large sample sizes as the system has proved to exhibit large fluctuations. Thus, estimates of  $\langle \gamma \rangle_s$  might be biased.

## 5. Summary and Conclusion

In this paper, we studied the spatial and temporal fluctuations of the number of moving particles per unit bed area, also called the particle activity [Furbish *et al.*, 2012a]. These fluctuations have been shown to have a great deal of effect on the measurements of bedload transport rates in both field and experimental surveys [Bunte and Abt, 2005; Cudden and Hoey, 2003; Garcia *et al.*, 2000; Dinehart, 1992; Gomez *et al.*, 1990]. The Eulerian model recently proposed by the authors [Ancey and Heyman, 2013] offers a simple theoretical framework to understand and quantify these fluctuations.

In that model, particle activity is shown to have a unique stationary average value, providing that the particle deposition rate is greater than their collective entrainment rate. However, the present paper has shown that locally particle activity evolves far from equilibrium, displaying large fluctuations around the mean. These fluctuations strongly depend on the spatial or temporal scale at which they are observed. Fluctuations are Poissonian at small scales; their amplitudes become larger than the mean for increasing scales; and eventually fluctuations reach a maximum at infinitely large scales. A characteristic length scale  $\ell_c = \sqrt{D/(\sigma - \mu)}$  emerges from the analysis of the spatial correlation function. For scales close to  $\ell_c$ , only 37% of the maximum possible fluctuations were observed. We also defined a local Péclet number  $Pe = \bar{u}_s \ell_c / D$  that describes the relative importance of advection against diffusion for particles at the correlation scale. This number plays an important role in the shape of the spatio-temporal correlation function.

Large endogenous fluctuations around the mean have also been reported for non-linear chemical systems that react and diffuse at the same time [Nicolis and Prigogine, 1971; Malek-Mansour and Nicolis, 1975; Gardiner *et al.*, 1976; Sornette, 2006; Schulz, 2008]. In these far from equilibrium systems, the microscopic fluctuations associated with the macroscopic state are not Poissonian as given by the theory of thermal equilibrium.

We compared our model with three experimental data sets, carried out under very different experimental conditions. Theoretical predictions agreed well with the experimental data. Note that in the model, only the free parameter  $\mu$  (or  $\lambda$ ) had to be tuned artificially to match the experiments; the others were calibrated independently. Nevertheless, it closely described the evolution of first- and second-order moments through space. The correlation length  $\ell_c$  is between 4 and 5 cm for the B and R experiments while H experiments show a longer correlation length ( $\ell_c = 15$  cm) because of smaller deposition rates. Local Péclet numbers in these experiments ranged between 2 and 17. This relatively large range shows that the main transport mode of particles can be very different from one experiment to another, depending on the shape and size of the particles as well as the bed slope and flow conditions. For instance, while in the B experiments particles are advected and diffused equally, in the R experiment particles are mostly advected by the fluid flow.

Another striking result of this study was the failure of the frozen-flow hypothesis. Although widely accepted and used

by researchers in fluid turbulence, it appears to be inaccurate when applied to bedload transport. If average quantities are conserved, no obvious link exists between spatial and temporal second-order moments. Thus, no firm conclusion can be drawn for the spatial fluctuations of particle activity when bedload is measured at a given location through time (for instance with sediment traps or geophones). Conversely, a picture of the spatial variation in particle activity cannot be easily related to the fluctuations of the solid discharge measured at a given location. Still, a relationship must exist and solving Eq. (27) could be of interest in overcoming this limitation in the future.

This study also provided interesting guidelines for researchers studying the fluctuations of bedload transport rates. We showed that an ideal design for an experimental setup should resolve scales equal to  $100\ell_c$  to capture 99% of the fluctuating behavior of particle activity. This suggests that for Böhm *et al.* [2004] experiments, a 4 m long observation window would be necessary. Note that, Ancey *et al.* [2008] considered the length necessary to fit the single cell model to be about  $22.5 \text{ cm} \ll 4 \text{ m}$ . However, we have shown that the variance does not reach its maximum value at this scale, so Ancey *et al.* [2008] model certainly under estimates fluctuations that would occur at scales longer than 22.5 cm. Furthermore, to accurately estimate the variance, several independent samples resolving this specific length scale have to be recorded. From these rough estimates, it is clear how difficult it becomes to get high quality measurements from such a wide range of scales. It is to be hoped that faster digital data transfer and massive storage capacity, coupled to modern imaging techniques, will soon overcome present limitations.

Another major issue to be addressed is the dependence of model parameters on external variables such as the bed slope, Froude number or shear velocity, etc. For simplicity, we took the parameters  $(\lambda, \mu, \sigma, \bar{u}_s, D)$  to be constant in time and space, but in reality nothing justifies this approximation. In natural rivers, stationary flow conditions are rarely met over long time periods. Moreover, bed-forms, bars and other morphological structures often develop in experimental flumes as well as in natural streams. As they modifying the flow locally, they also in turn modify the sediment transport process. The correlation length scale emerging from sediment transport might be comparable to the wavelength of these bed-forms so that non-trivial coupled phenomena might occur. No simple analytical treatment can be performed for parameters varying in space and time, so we must rely on numerical analysis. An example of such random simulations has been provided in our homogeneous case, but the generalization to more complicated cases is straightforward.

## Appendix A: Link to the “BCRE” model.

It is interesting to compare Eq. (7) to previous models of dry granular avalanches. For instance, the BCRE model first presented in *Bouchaud et al.* [1995] gives the density of rolling grains  $\mathcal{R}$  as the solution of:

$$\partial_t \mathcal{R} + \nabla(V\mathcal{R}) = \nabla^2(D\mathcal{R}) - \mathcal{R}\alpha\nabla h \quad (\text{A1})$$

where  $\nabla h$  stands for the bed slope variations close to the angle of repose and  $\alpha$  is a constant. Thus, in their model, when the slope is bigger than the angle of repose ( $\nabla h < 0$ ) the second term on the left-hand side acts as a source in the equation. The number of rolling grains is thus increases exponentially, leading to a local avalanche. On the contrary, when the slope is less than the angle of repose ( $\nabla h > 0$ ), grains are mainly deposited, causing the avalanche to stop ( $\mathcal{R} = 0$ ). The resemblance with Eq. (7) is striking. In the latter, an exponential increase in the number moving particles occurs when the collective motion parameter is greater than or equal to the deposition parameter ( $\mu \geq \sigma$ ). However, when deposition is greater than collective entrainment, a non trivial steady-state solution exists, due to the the particle entrainment process (with rate  $\lambda$ ).

As the entrainment of particles by a turbulent fluid is a random process [*Papanicolaou et al.*, 2002; *Valyrakis et al.*, 2010], our model could be seen as a “BCRE” model that includes a random perturbation. Though the present work concerns bedload transport, and we restrict ourselves to the steady-state case ( $\mu < \sigma$ ), the limit  $\mu \rightarrow \sigma$  might be of particular interest for other granular systems. Thus, we suggest that the stochastic model presented here may also be applicable to certain dry granular flows where interactions between moving grains are weak.

## Appendix B: Spatial correlation function

The equation for the stationary spatial correlation function in the Poisson variable  $g_s(r) = \langle \eta(x, t), \eta(x', t) \rangle_s$  reads:

$$D \frac{\partial^2 g_s(r)}{\partial r^2} - (\sigma - \mu)g_s(r) + \mu \langle \gamma \rangle_s \delta(r) = 0, \quad (\text{B1})$$

with  $r = |x - x'|$ . One can simplify Eq. (B1) by rescaling the variable  $r$  by  $\tilde{r} = r/\ell_c$  where  $\ell_c = \sqrt{D/(\sigma - \mu)}$ . It yields:

$$\frac{\partial^2 g_s(\tilde{r})}{\partial \tilde{r}^2} - g_s(\tilde{r}) + \frac{\langle \gamma \rangle_s}{\ell_c} \frac{\mu}{\sigma - \mu} \delta(\tilde{r}) = 0. \quad (\text{B2})$$

By means of Fourier transforms such that

$$g_s(\tilde{r}) = \frac{1}{2\pi} \int_{-\infty}^{+\infty} G(\omega) e^{i\omega\tilde{r}} d\omega,$$

and using the property

$$\delta(\tilde{r}) = \frac{1}{2\pi} \int_{-\infty}^{+\infty} e^{i\omega\tilde{r}} d\omega,$$

we obtain the algebraic equation:

$$G(\omega) = \frac{\langle \gamma \rangle_s}{\ell_c} \frac{\mu}{\sigma - \mu} \frac{1}{\omega^2 + 1}, \quad (\text{B3})$$

The Fourier inverse of Eq. (B3), is given by:

$$g_s(\tilde{r}) = \frac{\langle \gamma \rangle_s}{2\ell_c} \frac{\mu}{\sigma - \mu} \exp(-|\tilde{r}|). \quad (\text{B4})$$

Hence:

$$\langle \eta(x), \eta(x') \rangle_s = \frac{\langle \gamma \rangle_s}{2\ell_c} \frac{\mu}{\sigma - \mu} \exp\left(-\frac{|x - x'|}{\ell_c}\right). \quad (\text{B5})$$

## Appendix C: Spatio-Temporal correlation function

We want to solve the following equation:

$$\frac{\partial G(x, t)}{\partial t} = D \frac{\partial^2 G(x, t)}{\partial x^2} - \bar{u}_s \frac{\partial G(x, t)}{\partial x} - (\sigma - \mu)G(x, t), \quad (\text{C1})$$

with the initial condition  $G(x, 0)$  given by the solution of the stationary spatial correlation function, Eq. (14). Taking the dimensionless variables  $\tilde{t} = (\sigma - \mu)t$  and  $\tilde{x} = x/\ell_c$  one can simplify Eq. (C1):

$$\frac{\partial G(\tilde{x}, \tilde{t})}{\partial \tilde{t}} = \frac{\partial^2 G(\tilde{x}, \tilde{t})}{\partial \tilde{x}^2} - \text{Pe} \frac{\partial G(\tilde{x}, \tilde{t})}{\partial \tilde{x}} - G(\tilde{x}, \tilde{t}), \quad (\text{C2})$$

with  $\text{Pe} = \bar{u}_s \ell_c / D$ . Representing  $G(x, t)$  as a Fourier integral:

$$G(\tilde{x}, \tilde{t}) = \frac{1}{2\pi} \int_{-\infty}^{+\infty} \mathcal{G}(\omega, \tilde{t}) e^{i\omega\tilde{x}} d\omega,$$

Eq. (C2) becomes:

$$\frac{\partial \mathcal{G}(\omega, \tilde{t})}{\partial \tilde{t}} = -(\omega^2 + \text{Pe}i\omega + 1)\mathcal{G}(\omega, \tilde{t}). \quad (\text{C3})$$

The Fourier representation of the initial condition Eq. (14) is:

$$\mathcal{G}(\omega, 0) = \frac{\langle \gamma \rangle_s}{\ell_c} \left[ 1 + \left( \frac{\mu}{\sigma - \mu} \right) \frac{1}{\omega^2 + 1} \right], \quad (\text{C4})$$

so that the solution of Eq. (C3) is:

$$\mathcal{G}(\omega, \tilde{t}) = \mathcal{G}_d(\omega, \tilde{t}) + \mathcal{G}_r(\omega, \tilde{t}), \quad (\text{C5})$$

with :

$$\begin{aligned} \mathcal{G}_d(\omega, \tilde{t}) &= \frac{\langle \gamma \rangle_s}{\ell_c} \exp[-(\omega^2 + \text{Pe}i\omega + 1)\tilde{t}], \\ \mathcal{G}_r(\omega, \tilde{t}) &= \frac{\langle \gamma \rangle_s}{\ell_c} \frac{\mu}{\sigma - \mu} \frac{\exp[-(\omega^2 + \text{Pe}i\omega + 1)\tilde{t}]}{\omega^2 + 1}. \end{aligned} \quad (\text{C6})$$

The inverse Fourier transform of Eq.  $\mathcal{G}_d(\omega, \tilde{t})$  is easily found to be :

$$G_d(\tilde{x}, \tilde{t}) = \frac{\langle \gamma \rangle_s}{2\ell_c \sqrt{\pi\tilde{t}}} \exp\left[\frac{(\tilde{x} - \text{Pe}\tilde{t})^2}{4\tilde{t}} - \tilde{t}\right]. \quad (\text{C7})$$

Computing the inverse of  $\mathcal{G}_r(\omega, \tilde{t})$  is a more difficult task. The convolution property of Fourier transforms gives:

$$\mathcal{F}^{-1}\{F_1 \times F_2\} = f_1 * f_2, \quad (\text{C8})$$

where  $F_i$  is the Fourier transform of  $f_i$  and  $*$  the convolution operator.  $\mathcal{G}_r(\omega, \tilde{t})$  is the product of two functions whose Fourier inverses are:

$$\mathcal{F}^{-1}\left\{\frac{1}{\omega^2 + 1}\right\} = \frac{\exp(-|x|)}{2}, \quad (\text{C9})$$

$$\mathcal{F}^{-1}\{\exp[-\omega^2\tilde{t}]\} = \frac{\exp[-x^2/(4\tilde{t})]}{\sqrt{4\pi\tilde{t}}}, \quad (\text{C10})$$

so that the Fourier inverse of  $\mathcal{G}_r(\omega, \tilde{t})$  is given by:

$$G_r(\tilde{x} + \text{Pe}\tilde{t}, \tilde{t}) = \frac{\langle \gamma \rangle_s}{\ell_c} \frac{\mu}{\sigma - \mu} \frac{\exp(-\tilde{t})}{2\sqrt{4\pi\tilde{t}}} \cdot \int_{-\infty}^{+\infty} \exp(-|\tilde{x} - y|) \exp\left(\frac{-y^2}{4\tilde{t}}\right) dy. \quad (\text{C11})$$

Knowing the value of the following integrals:

$$\int_{-\infty}^x \exp(y) \exp\left(\frac{-y^2}{4t}\right) dy = \sqrt{\pi t} \exp(t) \text{erfc}\left(\frac{2t-x}{2\sqrt{t}}\right),$$

and

$$\int_x^{\infty} \exp(-y) \exp\left(\frac{-y^2}{4t}\right) dy = \sqrt{\pi t} \exp(t) \text{erfc}\left(\frac{2t+x}{2\sqrt{t}}\right),$$

where  $\text{erfc}$  is the complementary error function (e.g.  $\text{erfc}(x) = 1 - \text{erf}(x)$ ), one can obtain a general solution for Eq. (C11):

$$G_r(\tilde{x}, \tilde{t}) = \frac{\langle \gamma \rangle_s}{4\ell_c} \frac{\mu}{\sigma - \mu} \cdot \left\{ \exp(\tilde{x} - \text{Pe}\tilde{t}) \text{erfc}\left[\left(1 + \text{Pe}/2\right)\sqrt{\tilde{t}} + \tilde{x}/(2\sqrt{\tilde{t}})\right] + \exp(\text{Pe}\tilde{t} - \tilde{x}) \text{erfc}\left[\left(1 + \text{Pe}/2\right)\sqrt{\tilde{t}} - \tilde{x}/(2\sqrt{\tilde{t}})\right] \right\}. \quad (\text{C12})$$

## Appendix D: Spatial fluctuations

We wish to compute the integral:

$$\text{Var}[N(L, t)] = \int_L \int_L \langle \gamma(x, t), \gamma(x', t) \rangle dx dx'.$$

That is:

$$\text{Var}[N(L, t)] = \langle \gamma \rangle_s L + \frac{\langle \gamma \rangle_s}{2\ell_c} \frac{\mu}{\sigma - \mu} \int_{-L/2}^{L/2} \int_{-L/2}^{L/2} e^{-|x-x'|/\ell_c} dx dx'.$$

The value of the integral can be obtained by using:

$$\begin{aligned} & \int_{-L/2}^{L/2} \int_{-L/2}^{L/2} e^{|x-x'|/\ell_c} dx dx' = \\ & \int_{-L/2}^{L/2} \left[ \int_{-L/2}^x e^{(x-x')/\ell_c} dx + \int_x^{L/2} e^{-(x-x')/\ell_c} dx \right] dx' = \\ & \ell_c \int_{-L/2}^{L/2} \left[ 2 - e^{L/(2\ell_c)} \left( e^{-x'/\ell_c} + e^{x'/\ell_c} \right) \right] dx' = \\ & 2\ell_c^2 \left( L/\ell_c + e^{-L/\ell_c} - 1 \right). \end{aligned}$$

Thus:

$$\text{Var}[N(L, t)] = \langle \gamma \rangle_s L + \langle \gamma \rangle_s \ell_c \frac{\mu}{\sigma - \mu} \left( L/\ell_c + e^{-L/\ell_c} - 1 \right).$$

## Appendix E: Experimental dispersion index

From the individual particle trajectories, we define  $N(L, t)$  as the number of particles in a window of length  $L$ . To compare this with the theoretical result given in Eq.

(26), we compute the variance of  $N(L, t)$  as a function of the window size  $L$ .

In practice, we proceed as follows. For a given length scale, we randomly select  $n$  possible positions for the observation windows over the maximum length given by the camera resolution. Note that these sampling windows may possibly overlap each other if  $n$  or the length scale are large. The variance is then computed from the particles counts located in the  $n$  windows at each of the  $T$  recorded frames and for each of the  $n_e$  acquisitions. This sampling method gives a total sample of  $n \times n_e \times T \sim 300\,000$  values per length scales. It is worth mentioning that there are two reasons a high number of samples is needed to get accurate statistics: (i) sample values between frames are time-correlated, and (ii) observation windows are not always independent (for instance when the length scale approaches the maximum observation length, windows overlap).

Computing the temporal dispersion index follows roughly the same steps. We first randomly select  $n_1$  locations over the maximum observation window. Then, for each  $n_e$  acquisition, we construct the  $n_1 \times n_e$  time series of particle crossing those locations. For a given time scale and for each time series, we randomly select  $n_2$  time intervals inside the total experimental period and count the number of particle crossing events falling inside them. The temporal index is then computed by taking the variance of those interval counts, over a sample of  $n_1 \times n_e \times n_2 \sim 400\,000$  values.

## Notation

$\lambda$	Average particle entrainment rate per meter length in particles/m/s.
$\sigma$	Average particle deposition rate in $\text{s}^{-1}$ .
$\mu$	Average collective entrainment rate in $\text{s}^{-1}$ .
$d$	Local diffusivity in $\text{s}^{-1}$ .
$D$	Macroscopic diffusivity in $\text{m}^2/\text{s}$ .
$\bar{u}_s$	Mean particle velocity in m/s.
$\Delta x$	Cell length in m.
$N_i$	Number of moving particles in cell $i$ .
$\gamma(x, t)$	Density of moving particles at location $x$ and time $t$ in particles/m.
$\eta(x, t)$	Poisson density of moving particles at location $x$ and time $t$ in particles/m.
$\langle \gamma \rangle_s$	Steady-state homogeneous average density of moving particles in particles/m.
$\langle \eta \rangle_s$	Steady-state homogeneous average Poisson density of moving particles in particles/m.
$\ell_c$	Correlation length in m.
$t_c$	Correlation time in s in the frozen-flow hypothesis.
Pe	local Péclet number (non dimensional number).
$g$	Spatial correlation function.
$G$	Spatio-temporal correlation function.
$I$	Index of dispersion.
$K$	K-function.

**Acknowledgments.** This work was supported by the Swiss National Science Foundation under grant number 200021\_129538 (a project called ‘‘The Stochastic Torrent: stochastic model for bedload transport on steep slope’’), the R’Equip grant number 206021\_133831 and by the competence center in Mobile Information and Communication Systems (grant number 5005-67322, MICS project).

## References

- Ancey, C. (2010), Stochastic modeling in sediment dynamics: Exner equation for planar bed incipient bed load transport conditions, *J. Geophys. Res.*, *115*, F00A11.
- Ancey, C., and J. Heyman (2013), A microstructural approach to bedload transport: mean behaviour and fluctuations of particle transport rates, *J. Fluid Mech.*, *submitted*.
- Ancey, C., T. Bhm, M. Jodeau, and P. Frey (2006), Statistical description of sediment transport experiments, *Phys. Rev. E*, *74*(1), 011,302.
- Ancey, C., A. C. Davison, T. Böhm, M. Jodeau, and P. Frey (2008), Entrainment and motion of coarse particles in a shallow water stream down a steep slope, *J. Fluid Mech.*, *595*, 83–114.
- Baddeley, A. (2007), *Spatial Point Processes and their Applications, Lecture Notes in Mathematics*, vol. 1892, 1-75 pp., Springer Berlin Heidelberg, doi:10.1007/978-3-540-38175-4-1.
- Böhm, T., C. Ancey, P. Frey, J.-L. Reboud, and C. Ducottet (2004), Fluctuations of the solid discharge of gravity-driven particle flows in a turbulent stream, *Phys. Rev. E*, *69*(6), 061,307.
- Bouchaud, J.-P., M. E. Cates, J. R. Prakash, and S. F. Edwards (1995), Hysteresis and metastability in a continuum sandpile model, *Phys. Rev. Lett.*, *74*(11), 1982–1985.
- Bunte, K., and S. R. Abt (2005), Effect of sampling time on measured gravel bed load transport rates in a coarse-bedded stream, *Water Resour. Res.*, *41*(11), W11,405, doi:10.1029/2004WR003880.
- Celik, A., P. Diplas, C. Dancy, and M. Valyrakis (2010), Impulse and particle dislodgement under turbulent flow conditions, *Phys. Fluids*, *22*(4), 046,601.
- Chaturvedi, S., and C. Gardiner (1978), The poisson representation. ii two-time correlation functions, *J. Stat. Phys.*, *18*, 501–522, doi:10.1007/BF01014520.
- Cox, D. R., and V. Isham (1980), *Point Processes*, Monograph on applied statistics and probability 12, doi:0-412-21910-7.
- Cudden, J. R., and T. B. Hoey (2003), The causes of bedload pulses in a gravel channel: the implications of bedload grain-size distributions, *Earth Surf. Processes*, *28*(13), 1411–1428, doi:10.1002/esp.521.
- Detert, M., V. Weitbrecht, and G. H. Jirka (2010), Laboratory measurements on turbulent pressure fluctuations in and above gravel beds, *J. Hydraul. Eng.*, *136*(10), 779–789.
- Dinehart, R. L. (1992), Evolution of coarse gravel bed forms: Field measurements at flood stage, *Water Resour. Res.*, *28*(10), 2667–2689, doi:10.1029/92WR01357.
- Drake, T. G., R. L. Shreve, W. E. Dietrich, P. J. Whiting, and L. B. Leopold (1988), Bedload transport of fine gravel observed by motion-picture photography, *J. Fluid Mech.*, *192*(JUL), 193–217.
- Dwivedi, A., B. W. Melville, A. Y. Shamseldin, and T. K. Guha (2011), Analysis of hydrodynamic lift on a bed sediment particle, *J. Geophys. Res.-earth*, *116*(F2), F02,015, doi:10.1029/2009JF001584.
- Einstein, H. (1937), *Der Geschiebetrieb als Wahrscheinlichkeitproblem Bedload transport as a probability problem*, English translation by W.W. Sayre, in Sedimentation, Ed. H.W. Shen, Fort Collins, Colorado, 1972, C1–C105, ETHZ.
- Einstein, H. A. (1950), *The bed-load function for sediment transportation in open channel flows*, Tech. Bul. No. 1026, U.S. Dept. of Agriculture, Washington, D. C.
- Furbish, D. J., and M. W. Schmeeckle (2013), A probabilistic derivation of the exponential-like distribution of bed load particle velocities, *Water Resour. Res.*, *49*(3), 1537–1551, doi:10.1002/wrcr.20074.
- Furbish, D. J., P. K. Haff, J. C. Roseberry, and M. W. Schmeeckle (2012a), A probabilistic description of the bed load sediment flux: 1. theory, *J. Geophys. Res.-earth*, *117*(F3), F03,031–, doi:10.1029/2012JF002352.
- Furbish, D. J., A. E. Ball, and M. W. Schmeeckle (2012b), A probabilistic description of the bed load sediment flux: 4. fickian diffusion at low transport rates, *J. Geophys. Res.-earth*, *117*(F3), n/a–n/a, doi:10.1029/2012JF002356.
- Garcia, C., J. B. Laronne, and M. Sala (2000), Continuous monitoring of bedload flux in a mountain gravel-bed river, *Geomorphology*, *34*(12), 23 – 31, doi:http://dx.doi.org/10.1016/S0169-555X(99)00128-2.
- Gardiner, C., and S. Chaturvedi (1977), The poisson representation. i. a new technique for chemical master equations, *J. Stat. Phys.*, *17*, 429–468, doi:10.1007/BF01014349.
- Gardiner, C., K. McNeil, D. Walls, and I. Matheson (1976), Correlations in stochastic theories of chemical reactions, *J. Stat. Phys.*, *14*, 307–331, doi:10.1007/BF01030197.
- Gardiner, C. W. (2002), *Handbook of stochastic methods : for physics, chemistry and the natural sciences*, Springer series in synergetics, 13, Springer.
- Gillespie, D. (1991), *Markov Processes: An Introduction for Physical Scientists*, Academic Press.
- Gomez, B., D. W. Hubbell, and H. H. Stevens (1990), At-a-point bed load sampling in the presence of dunes, *Water Resour. Res.*, *26*(11), 2717–2731, doi:10.1029/WR026i011p02717.
- Heyman, J., F. Mettra, H. B. Ma, and C. Ancey (2013), Statistics of bedload transport over steep slopes: Separation of time scales and collective motion, *Geophys. Res. Lett.*, *40*(1), 128133, doi:10.1029/2012GL054280.
- Hill, K. M., L. DellAngelo, and M. M. Meerschaert (2010), Heavy-tailed travel distance in gravel bed transport: An exploratory enquiry, *J. Geophys. Res.*, *115*, F00A14.
- Hoey, T. (1992), Temporal variations in bedload transport rates and sediment storage in gravel-bed rivers, *Prog Phys Geog*, *16*(3), 319–338.
- Jensen, E. B. V., and L. S. Nielsen (2001), A review on inhomogeneous markov point processes, *Lecture Notes-Monograph Series*, *37*, pp. 297–318.
- Jerolmack, D. J., and D. Mohrig (2005), A unified model for subaqueous bed form dynamics, *Water Resour. Res.*, *41*(12), n/a–n/a, doi:10.1029/2005WR004329.
- Kloeden, P. E., and E. Platen (2011), *Numerical Solution of Stochastic Differential Equations*, Springer, New York.
- Kuhnle, R. A., and J. B. Southard (1988), Bed load transport fluctuations in a gravel bed laboratory channel, *Water Resour. Res.*, *24*(2), 247–260.
- Lajeunesse, E., L. Malverti, and F. Charru (2010), Bed load transport in turbulent flow at the grain scale: Experiments and modeling, *J. Geophys. Res.*, *115*(F4), F04,001.
- Malek-Mansour, M., and G. Nicolis (1975), A master equation description of local fluctuations, *J. Stat. Phys.*, *13*, 197–217, doi:10.1007/BF01012838.
- Martin, R. L., D. J. Jerolmack, and R. Schumer (2012), The physical basis for anomalous diffusion in bed load transport, *J. Geophys. Res.-earth*, *117*(F1), n/a–n/a, doi:10.1029/2011JF002075.
- Nicolis, G., and I. Prigogine (1971), Fluctuations in nonequilibrium systems, *Proc. Natl. Acad. Sci. U. S. A.*, *68*(9), 2102–2107.
- Nikora, V., H. Habersack, T. Huber, and I. McEwan (2002), On bed particle diffusion in gravel bed flows under weak bed load transport, *Water Resour. Res.*, *38*(6), 1081.
- Ogata, Y. (1999), Seismicity analysis through point-process modeling: A review, *Pure Appl Geophys*, *155*(2-4), 471–507, doi:10.1007/s000240050275.

- Papanicolaou, A. N., P. Diplas, N. Evaggelopoulos, and S. Fotopoulos (2002), Stochastic incipient motion criterion for spheres under various bed packing conditions, *J. Hydraul. Eng.*, *128*(4), 369–380.
- Rickenmann, D., J. M. Turowski, B. Fritschi, A. Klaiber, and A. Ludwig (2012), Bedload transport measurements at the erlenbach stream with geophones and automated basket samplers, *Earth Surf. Processes*, *37*(9), 1000–1011, doi:10.1002/esp.3225.
- Ripley, B. (1976), The second order analysis of stationary point processes, *J. Appl. Probab.*, *13*, 255–266.
- Rogers, S., T. Waigh, X. Zhao, and J. Lu (2007), Precise particle tracking against a complicated background: polynomial fitting with gaussian weight, *Phys Biol*, *4* (3), 220.
- Roseberry, J. C., M. W. Schmeeckle, and D. J. Furbish (2012), A probabilistic description of the bed load sediment flux: 2. particle activity and motions, *J. Geophys. Res.-earth*, *117*(F3), n/a–n/a, doi:10.1029/2012JF002353.
- Schulz, M. (2008), Chemical reactions and fluctuations, *Eur. Phys. J. Special Topics*, *161*(1), 143–150, doi:10.1140/epjst/e2008-00756-1.
- Singh, A., K. Fienberg, D. J. Jerolmack, J. Marr, and E. Foufoula-Georgiou (2009), Experimental evidence for statistical scaling and intermittency in sediment transport rates, *J. Geophys. Res.*, *114*(F1), F01,025.
- Sornette, D. (2006), *Critical Phenomena in Natural Sciences: Chaos, Fractals, Selforganization and Disorder: Concepts and Tools*, 2nd ed., Springer.
- Taylor, G. I. (1922), Diffusion by continuous movements, *Proc. London Math. Soc.*, *20*, 196212.
- Valyrakis, M., P. Diplas, C. L. Dancey, K. Greer, and A. O. Celik (2010), Role of instantaneous force magnitude and duration on particle entrainment, *J. Geophys. Res.*, *115*(F2), F02,006–.
- Van Kampen, N. G. (2007), *Stochastic Processes in Physics and Chemistry*, 3 ed., North Holland.
- Wu, F., and Y. Chou (2003), Rolling and lifting probabilities for sediment entrainment, *J. Hydraul. Eng.*, *129*(2), 110–119, doi:10.1061/(ASCE)0733-9429(2003)129:2(110).
- Yilmaz, A., O. Javed, and M. Shah (2006), Object tracking: A survey, *ACM Comput. Surv.*, *38*(4), doi:10.1145/1177352.1177355.

---

Corresponding author: J. Heyman, EPFL - LHE Station 18, 1015 Lausanne. (joris.heyman@epfl.ch)